aerospace

MDPI

Article

Turbulent Boundary Layer Separation Control Using Magnetohydrodynamic Plasma Actuator

Alexander Kotvitskii, Pavel Kazanskii and Ivan Moralev *

Joint Institute for High Temperatures RAS, Izhorskaya Str, 13 bld.2, Moscow 127415, Russia; alex.kotvitsky00@gmail.com (A.K.); fokoo@yandex.ru (P.K.)
* Correspondence: morler@mail.ru

Abstract: The pulse electric arc discharge in an external magnetic field is studied as a vortex generator in the subsonic boundary layer. A pulsed Ampere force induces a hairpin vortex near the wall; its structure depends on the relative direction of arc propagation and external flow velocity. The data presented in this article were obtained from parametric studies of vortex characteristics and their effects on the boundary layer profile at various actuator momentum coefficients ($C_\mu = 1 - 30$) and vortex sizes relative to the boundary layer thickness ($D/\delta = 0.5 - 1.2$). Also, the control of turbulent boundary layer separation on a bump at a flow velocity up to 50 m/s was attempted. An average shift of the separation line by 15% of the bump height was obtained at a flow velocity of 50 m/s and a total momentum coefficient of 0.6%.

Keywords: turbulent boundary layer; flow separation control; plasma vortex generator; arc discharge; magnetohydrodynamics

Citation: Kotvitskii, A.; Kazanskii, P.; Moralev, I. Turbulent Boundary Layer Separation Control Using Magnetohydrodynamic Plasma Actuator. *Aerospace* **2023**, *10*, 907. https://doi.org/10.3390/aerospace10110907

Academic Editor: Kung-Ming Chung

Received: 5 September 2023
Revised: 18 October 2023
Accepted: 20 October 2023
Published: 25 October 2023

1. Introduction

Plasma actuators are widely studied as an alternative to mechanical and fluidic devices in flow control problems [1–3]. A significant proportion of the results in this area have been obtained for boundary layer separation control. Separation delay using plasma actuators was demonstrated for airfoil stall conditions both in static [4,5] and dynamic conditions [6,7]. More recently, some in-flight tests for UAV vehicles were performed [8,9]. One should note that successful attempts to suppress separation using plasma actuators were performed either at extremely low flow velocities [4] or in stall conditions, when the boundary layer is laminar at the separation point [5,10].

Extensive research over decades has been performed on the optimization of canonical vortex generators capable of creating large-scale vortices in the boundary layer [11]. Vortex generators usually pursue the goal of enhancing the kinematic transport of high-momentum fluid from the potential flow core towards the wall. The magnitude of actuator-induced vortices should be at least comparable to the typical magnitude of natural turbulent pulsations in a boundary layer, that is, in the order of 0.1 U_0. The required size of the vortices varies from 0.5 to $2\delta_1$. Therefore, active control of the high-velocity turbulent boundary layer demands a significant actuation amplitude.

Boundary layer separation control using plasma actuators was studied for AC dielectric barrier discharge actuators [7,12–14], nanosecond surface discharge actuators [5,15] and SparkJets [16]. It is commonly assumed that separation delay is achieved via the addition of momentum to the boundary layer and vortex formation. However, thrust generated by DBD actuators is limited to 100 mN/m [17,18], and thus, TBL separation has mostly been demonstrated for flow velocities below 20 m/s. The results obtained for leading edge separation at higher flow velocities are attributed to tripping of the boundary layer or excitation of the shear layer at the edge of the separation zone. A higher forcing level can be obtained using thermal plasma actuators ("SparkJets") [19,20]. These devices create a high-velocity jet at the exit of a small discharge cavity installed in the streamlined wall. The

jet velocity can be as high as 500 m/s, thus allowing the control of high-speed flows. It has been shown that, depending on the injection parameter, a wall-normal pulsed jet generates in a boundary layer either a vortex ring or a hairpin vortex [21]. Still, the need to refill the cavity after the pulse limits the operation frequency of the SparkJet system by several kHz. Finally, an adaptive vortex generator, designed as a submerged wedge actuated by spark discharge, is proposed in [22] for turbulent boundary layer control at supersonic velocities.

MHD interaction in magnetically driven arcs was also considered for flow control [23]. At a current of 100 A, and a magnetic field of 1T, the typical Ampere force induced in the discharge is as high as 100 H/m. The efficiency of flow acceleration can be as high as 2–3%, exceeding the efficiency of DBD or corona discharge by more than an order of magnitude. The flow structure around a magnetically driven arc was studied in [24,25], and recently, in more detail in [26,27]. It was shown that inside the conductive channel and in its close vicinity, two counter-rotating vortices are formed, driven by the inhomogeneity of the magnetic force. When the arc is initiated near the wall, the near-wall vortex dissipates, and a single vortex filament is left (Figure 1, [27]). When the pulsed arc is initiated in the homogeneous magnetic field, the vortex filament has a hairpin shape, ending at the electrodes. Arc discharges in the magnetic field were considered for separation control at various flow velocities [23,28]. Still, no systematic studies of the details of MHD actuator operation have been carried out. The interaction of the pulsed arc with a boundary layer is essentially three-dimensional. Natural shear affects both the shape of the arc filament and the dynamics of the arc-induced vortices. The arc discharge leaves a relatively large heated cavern, limiting the minimal size of the induced vortices. This means that the size of the disturbances relative to the boundary layer thickness is also a nontrivial factor affecting the resulting flow structure. These issues, together with a direct attempt to control the boundary layer separation by arc-based MHD actuators, are the major object of study in the present work.

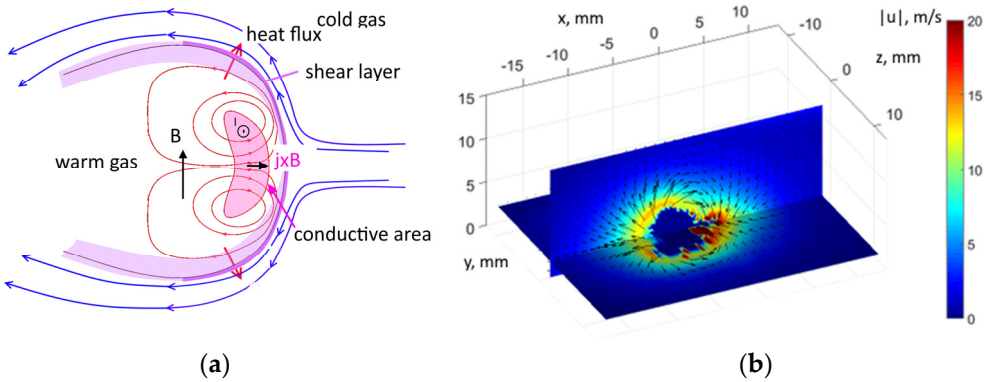

Figure 1. Structure of the flow, induced by magnetically driven arc in quiescent air: (**a**) principal scheme of the MHD interaction region [26]; (**b**) three-dimensional flow field, 500 µs [27].

The main goal of this work is to study the magnetically driven arc actuator as a flow control device for turbulent boundary layer separation control. Arc discharge in a wall-normal magnetic field is created in the turbulent boundary layer at a flow velocity up to 80 m/s. The flow structure in the vicinity of the arc is studied via PIV. Secondary deformation of the boundary layer downstream of the arc is measured and quantified by assessing displacement thickness change. Finally, the separation control of the boundary layer in the region of the adverse pressure gradient is demonstrated.

The paper is structured as follows. In Section 2, the experimental setup and the boundary layer properties are described. Section 3 describes the experimental data, immediately followed by the discussion. The paper is concluded with a short summary.

2. Experimental Details

All experiments were carried out at a subsonic velocity of 20–80 m/s in a D-2 wind tunnel at JIHT RAS with a cross-section of 100 × 100 mm. A 2D bump was installed on the test section (Figure 2a). The length of the straight section of the bump was 300 mm, enough to assume a zero local pressure gradient in its central part. On its downstream side, separation occurred. Two measurement configurations were used in this experiment. For the detailed study of the interaction of plasma actuator-induced disturbances with the oncoming flow, electrodes were installed on the straight wall (Figure 2b). In the boundary layer separation control experiments, electrodes were shifted to the trailing part of the bump, closer to the separation point (Figure 2c). This led to an increase in the actuator's performance.

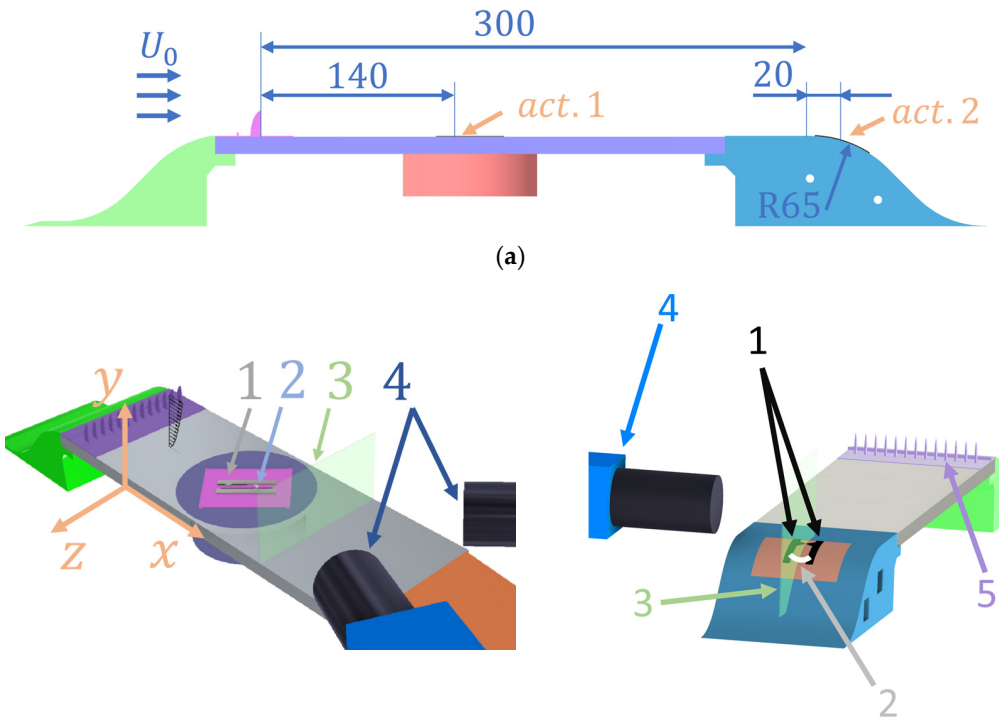

Figure 2. Scheme of the aerodynamic experiment. (**a**) Bump construction and actuator placement. (**b**) Scheme of the PIV setup used for the detailed study of the arc–boundary layer interaction. (**c**) Scheme of the separation control experiment. 1—electrodes, 2—arc, 3—laser sheet, 4—CCD cameras, 5—obstacle array in the boundary layer.

In natural conditions, the boundary layer was turbulent in the whole area of the bump at all flow velocities. The velocity profile is shown in Figure 3. The displacement thickness of the natural boundary layer was $\delta_1 \sim 0.74$ mm, and the shape factor was $H_{12} \sim 1.3$. To analyze the role of the relation between the disturbance size and boundary layer thickness, BL thickness was artificially increased via an obstacle array immediately after the end of the contraction section. The obstacle array was designed following [29] and was composed of a pyramid-like vortex generator 10 mm high, a 1 mm 2D step and a 10 mm wide rough strip. The thickness of the artificial boundary layer was $\delta_1 \sim 2.6$ mm.

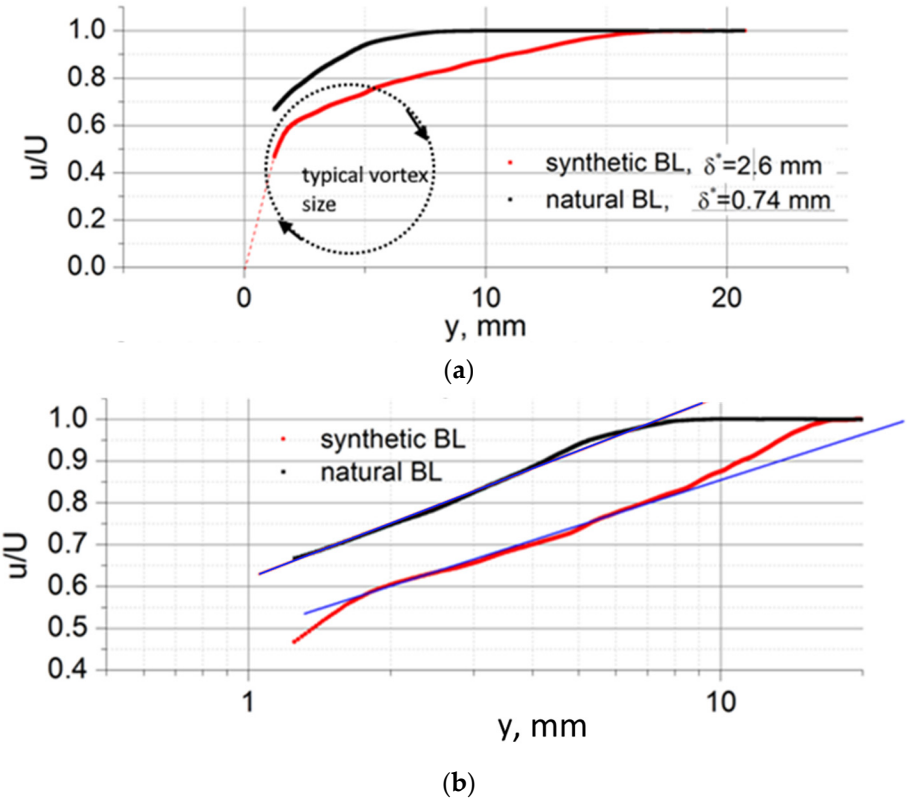

Figure 3. Boundary layer profiles in natural and artificial cases at (**a**) linear scale and (**b**) logarithmic scale. Straight lines show the logarithmic law.

2.1. Separation Control Experiment

Turbulent flow separation was carried out on the smooth backward side of the bump (Figure 2c). The bump's trailing section profile in its initial part can be approximated by a cylinder with a radius of 64 mm. Experiments were carried out at free-stream flow velocity from 20 to 50 m/s. In all cases, the thickness of the boundary layer was artificially increased using an obstacle array. The actuator was installed at a position 20 mm downstream of the trailing bump section start. Electrodes were installed at a zero sweep angle α to the oncoming flow. The arc breakdown position was chosen to be slightly upstream of the average separation point in the reference conditions. Flow measurements were performed on a symmetrical plane between the electrodes.

2.2. Particle Imaging Velocimetry

Flow structure was studied using the stereo LaVision Flow Master PIV system at a frame rate of 7 Hz. To study the flow dynamics, measurements were taken at a fixed delay from the discharge initiation moment. Data were averaged over 50 frames in the boundary layer experiment and up to 500 frames in the separation region. The flow was seeded by DEHS droplets upstream of the wind tunnel contraction. The typical dynamic relaxation time for the droplets was estimated to be 0.15–0.5 μs, and was verified via velocity measurements behind the shock front to be within 2 μs.

Particle images were taken either on the XY (co-flow) or YZ (cross-flow) planes; 4 Mpix CCD cameras were used for image acquisition. Single-camera 2D measurements were performed to accurately measure the longitudinal velocity distribution in a boundary layer or visualize the dynamics of a separation point. To study the disturbance structure, a stereo PIV setup was used, with two cameras set at an angle of about 30 deg to the flow direction. Stereo measurements were performed on the YZ plane, at equidistant positions, with a step of 0.5 mm. The in-plane resolution of PIV measurements was 0.12–0.2 mm.

PIV data were processed using a cross-correlation algorithm with a typical window size of 32 × 32 pix and 50% window overlap. The typical error of the individual velocity measurement was in the order of 3%. Pulse-to-pulse variation in the arc structure in the turbulent environment, together with turbulent pulsations, led to a velocity RMS in the order of 15%. The statistics used led to approximately a 3% error for the average velocity flow field.

2.3. Plasma Actuator

Arc discharge was initiated on a ceramic insert, mounted flush with the wall (Figure 4a). The voltage was applied to a pair of tungsten foil electrodes (1 and 2), shaped as rails with triangular sharpeners, for the discharge initiation. To trigger the breakdown, an additional electrode (3) was used, buried in silicon under the ceramic surface. The distance between the electrodes was 11 mm, and the sharpeners were separated by a 3 mm gap. The wall-normal magnetic field was created usinh a permanent magnet, placed under the surface. The typical field strength at 1 mm above the wall was 0.3 T. The construction of the discharge system mount allowed it to vary the sweep angle of the electrodes relative to the flow.

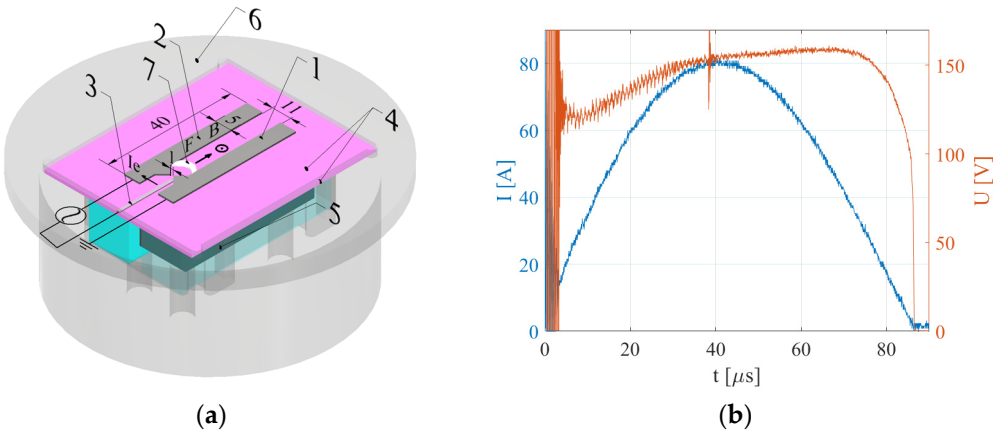

(**a**) (**b**)

Figure 4. (**a**) Plasma actuator design: 1—cathode, 2—anode, 3—initiating electrode, 4—ceramic plate, 5—permanent magnet, 6—case, 7—arc discharge. (**b**) Current and voltage traces during the discharge pulse.

The voltage between the electrodes and arc current is shown in Figure 4b. The discharge was powered by a half-sinuous current pulse with a peak current of 80 A and a duration of 80 μs. The total dissipated energy was estimated as 670 mJ; the total transferred charge was 4.5 mC per pulse. The pulse repetition rate was varied from 1 Hz in the vortex visualization experiments to 700 Hz in the separation control tests.

The peak Ampere force value at the current maximum was estimated as 24 N. The local momentum coefficients based on this value and boundary layer displacement thickness are summarized in Table 1.

Table 1. Actuator peak momentum coefficient $C_\mu = IB/(\rho U_0{}^2 \delta_1)$ at various tested flow velocities and boundary layer thicknesses.

U_0 (m/s)	δ_1 = 0.74 mm	δ_1 = 2.60 mm
20.00	$C_\mu = 62$	$C_\mu = 18$
50.00	no tests	$C_\mu = 2.8$
80.00	no tests	$C_\mu = 1.1$

3. Results

3.1. Vortices Induced by MHD Actuator in a Boundary Layer

A detailed study of the disturbance structure was performed in the natural boundary layer at 20 m/s. Disturbances induced by the pulsed arc were studied at various electrode sweep angles from $\alpha = 0$ (arc moves in a co-flow direction) to π (arc moves in a counterflow direction). For these conditions, the flow structure was reconstructed by scanning the area along the *z*-axis for a fixed time delay of 1 ms. Figure 5 shows the visualization of the arc-induced vortex using the longitudinal component of vorticity and Q-criterion.

As was shown in [28], in quiescent conditions, the pulsed arc in the magnetic field generates a hairpin vortex near the wall. External shear present in the boundary layer significantly affects the vortex shape, with its deformation depending on the vortex orientation relative to the flow.

At $\alpha = 0$, when the arc filament is driven by magnetic force in the flow direction, the general structure of the disturbance is conserved, and the disturbance structure can still be described as a hairpin vortex (Figure 5a). Shear leads to stretching of the vortex legs. The typical elevation of the vortex head above the wall appears to be 3 mm; thus, it is positioned in the upper part of the boundary layer. The peak velocity in the vortex core at t = 1 ms can be estimated from the vertical component as 8 m/s = 0.38 U_0 and is obtained at a position 2 mm from the vortex center. The peak vorticity value is $6 \times 10^3 \cdot 1/s^2$.

An increase in the electrode sweep angle leads to pronounced asymmetry of the induced vortex. The typical disturbance structure measured at $\alpha = \pi/4$ is shown in Figure 5b. One can see that the horseshoe vortex is twisted, with the downstream "leg" formed closer to the wall. Because of a higher viscous force, the amplitude of this vortex is reduced.

A further increase in the sweep angle leads to a reduction in the transversal size of the disturbance. Due to the closer position of the vortex legs, further twisting of the vortex pair is observed ($\alpha = \pi/2$, Figure 5c).

As one increases the sweep angle above the value $\pi/2$, the situation is inverted. The initial horseshoe vortex left after the MHD interaction spans in a counterflow direction. As a result, convection in the boundary layer leads to compression of the disturbance (Figure 5d,e).

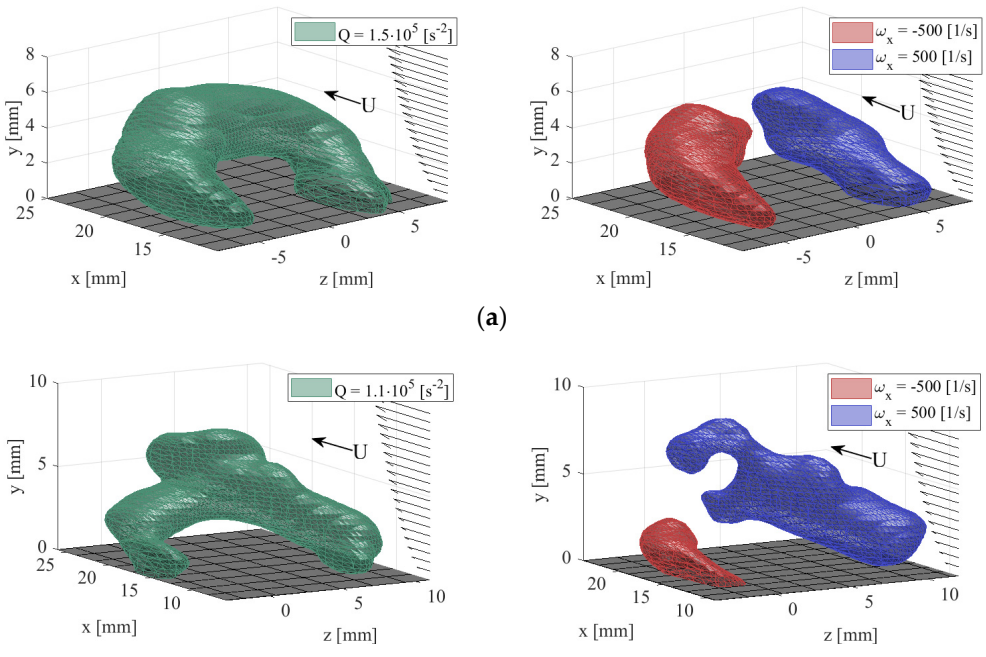

Figure 5. *Cont.*

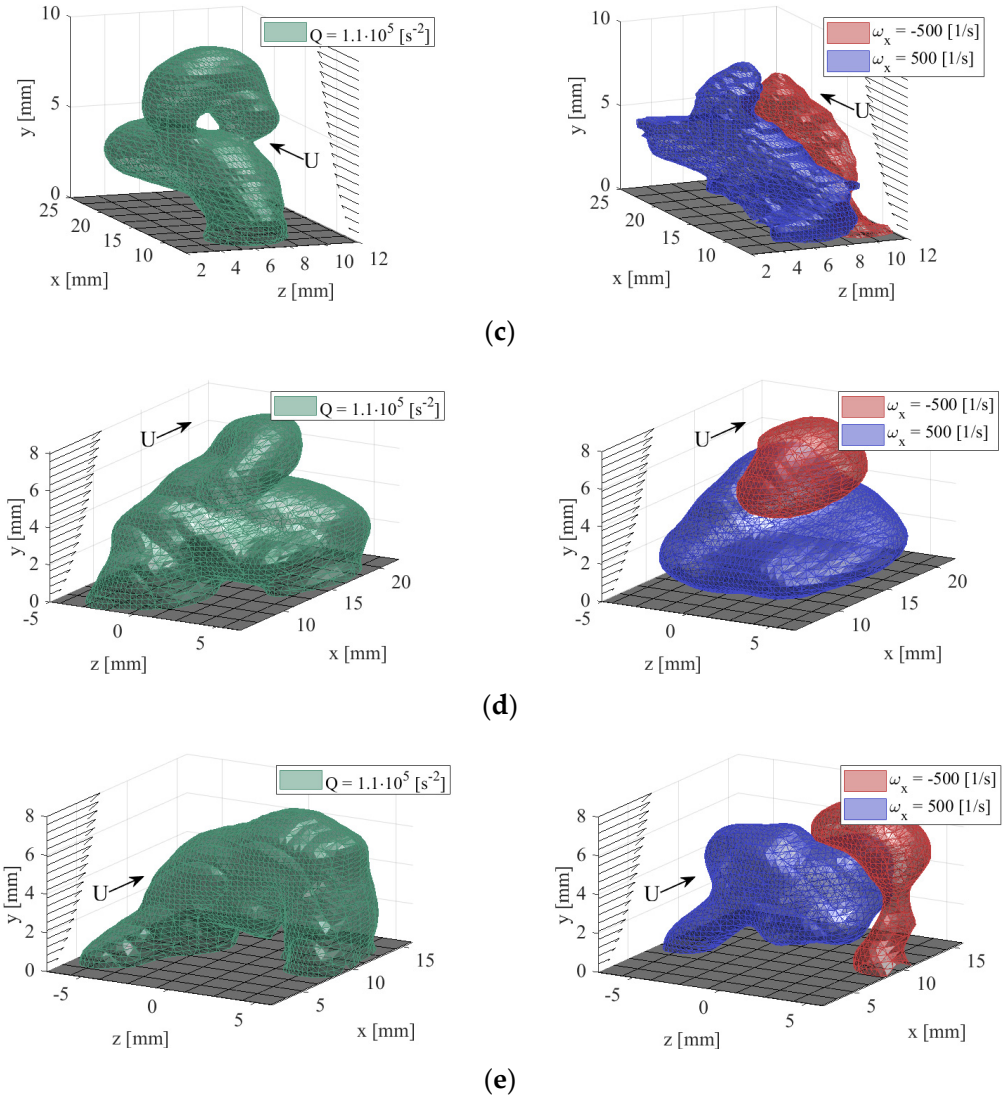

Figure 5. Vortex induced by pulsed arc discharge in a magnetic field in the boundary layer. Flow is visualized via Q-criterion (**left**) and by longitudinal vorticity component (**right**). Time delay is t = 1 ms after pulse initiation. Electrode sweep angles: (**a**) $\alpha = 0$, (**b**) $\alpha = \pi/4$, (**c**) $\alpha = \pi/2$, (**d**) $\alpha = 3\pi/4$, (**e**) $\alpha = \pi$.

3.2. Vortex Evolution in Boundary Layer

Vortex evolution in the boundary layer was studied at an electrode sweep angle of $\alpha = \pi/2$. As was shown above, the discharge-induced disturbance at a sufficiently big delay is composed of two counter-rotating longitudinal vortices, starting at the electrodes, and then, convected and stretched by the boundary layer flow. For the non-zero sweep angle, the vortices are formed at various heights in the boundary layer. When the arc is swept in the direction normal to the oncoming flow ($\alpha = \pi/2$), this asymmetry is maximal. The main features of disturbance evolution that can be seen in Figure 6 are vortex stretching in the shear flow and its decay. The vortex filament located closer to the wall dissipates in 2 ms, and a single vortex filament, aligned with the flow and ending at the wall, is left in the boundary layer.

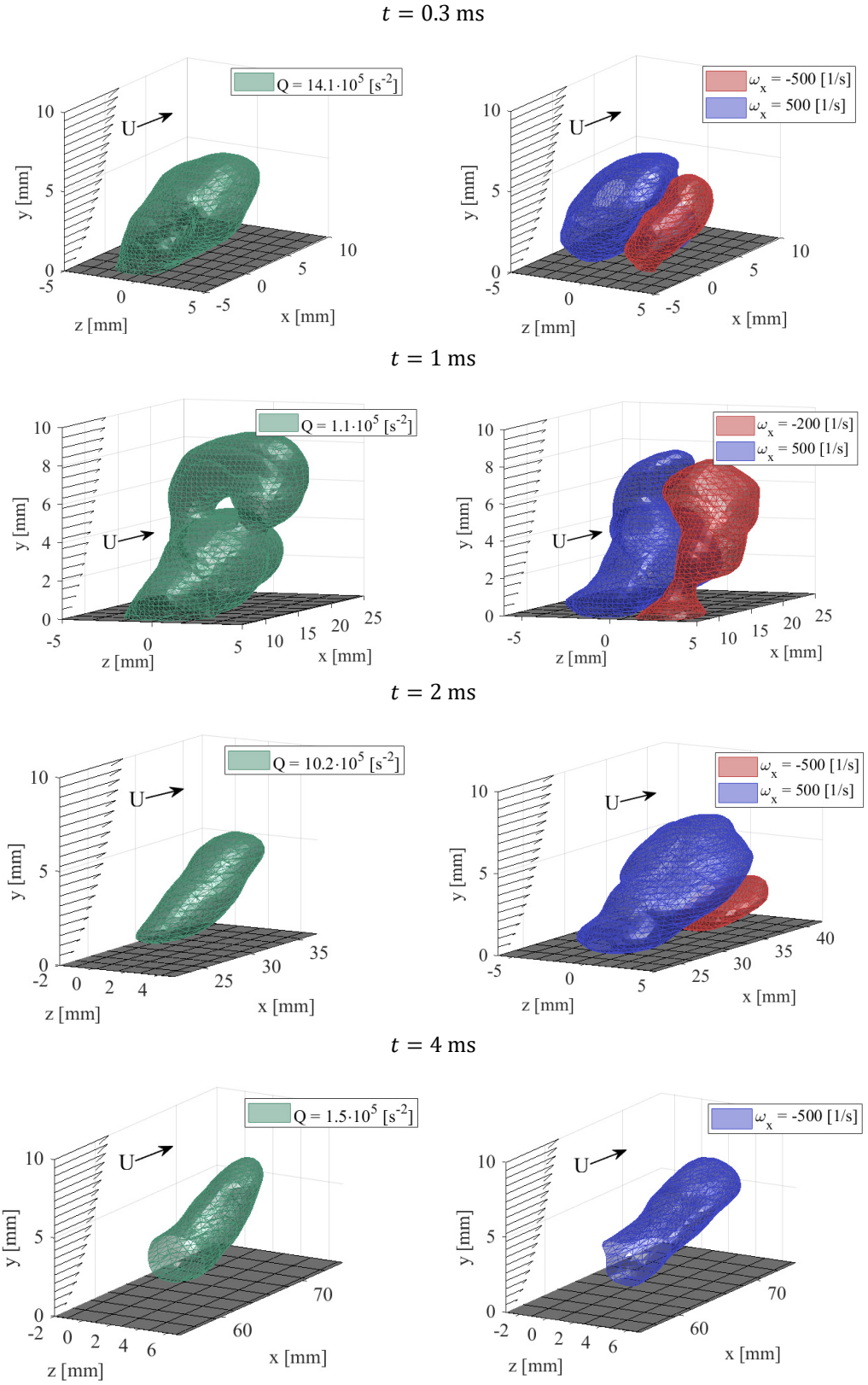

Figure 6. Evolution of the vortex structure at $\alpha = \pi/2$ (right—Q-criteria isosurface, left—longitudinal vorticity isosurface).

The vortex dissipation can be characterized by a reduction in circulation, associated with the upper and lower vortex filaments Γ^+ and Γ^-. These values were calculated as the integrals of positive and negative vorticity in the cross-flow planes:

$$\Gamma^+ = \int_S \omega_x H(\omega_x) dxdy, \quad (1)$$

where H represents the step function.

The evolution of the circulation along the vortex line is shown in Figure 7. One can see that as the vortex is convected downstream, the maximal circulation value diminishes. The circulation distributions along x are broadened due to the vortex stretching in the boundary layer. Finally, one can see that the lower vortex dissipates more rapidly in comparison to the upper one, due to the higher turbulent dissipation near the wall.

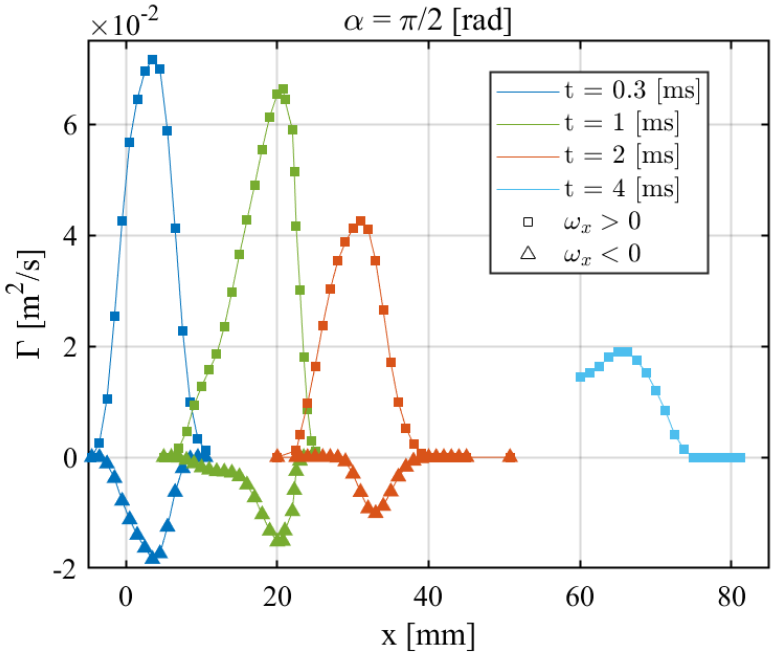

Figure 7. Longitudinal component of circulation in vortex filaments at consequent time moments.

3.3. Boundary Layer Modification by Arc-Induced Vortices

The pattern left in the boundary layer depends on the shape and dynamics of the induced vortices. According to the Navier–Stokes equations, two mechanisms can be responsible for boundary layer profile modification by a plasma actuator: initial acceleration of the flow during arc propagation, and kinematic momentum transport in the boundary layer. A comparison of the longitudinal velocity deformation in the boundary layer is given below for various electrode sweep angles.

The distribution of the stream-wise velocity in the cross-flow plane is shown in Figure 8. For $\alpha = 0$, the boundary layer becomes thinner in the central part and thicker in the outer part of the disturbed region. The regions with velocity excess and deficit correspond to the wall-normal velocity direction in the hairpin vortex. For the nonzero sweep angle, the flow deformation becomes asymmetric; the vortex head induces stronger deformation of the boundary layer at the corresponding lateral side of the disturbance. For the upstream propagating arc, the boundary layer becomes thicker in the whole disturbed region.

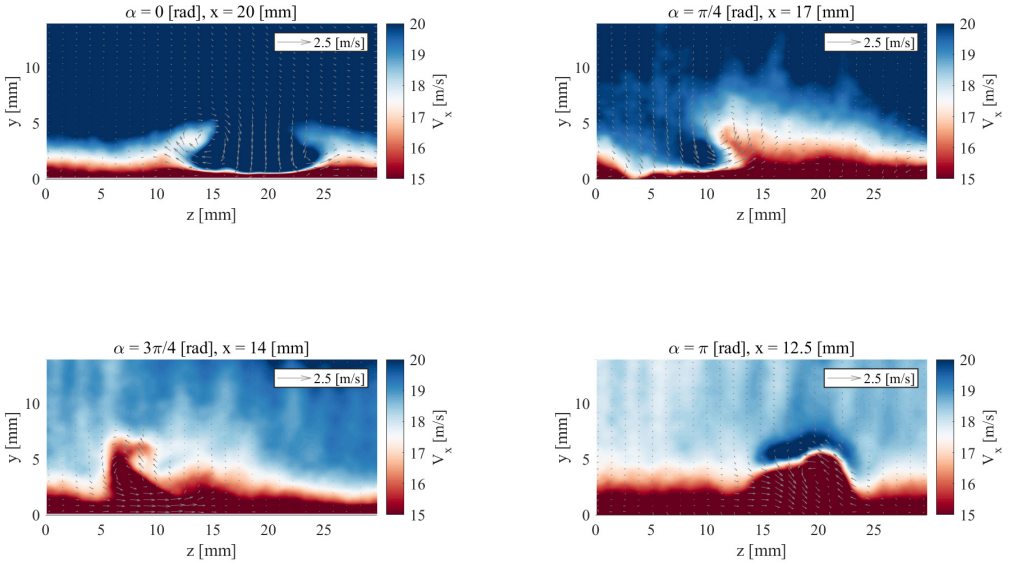

Figure 8. Longitudinal flow component in the disturbed boundary layer at t = 1 ms after discharge breakdown.

Local displacement thickness δ_1 was used as an integral parameter characterizing boundary layer deformation (Figure 9). For an electrode sweep angle of zero, minimal thickness is obtained between the horseshoe vortex legs, decreasing from 0.76 mm in the unperturbed case down to 0.45 at the minimal point. Due to the lift-up of the low-speed fluid from the wall, the boundary layer becomes thicker at the front and lateral sides of the disturbed region.

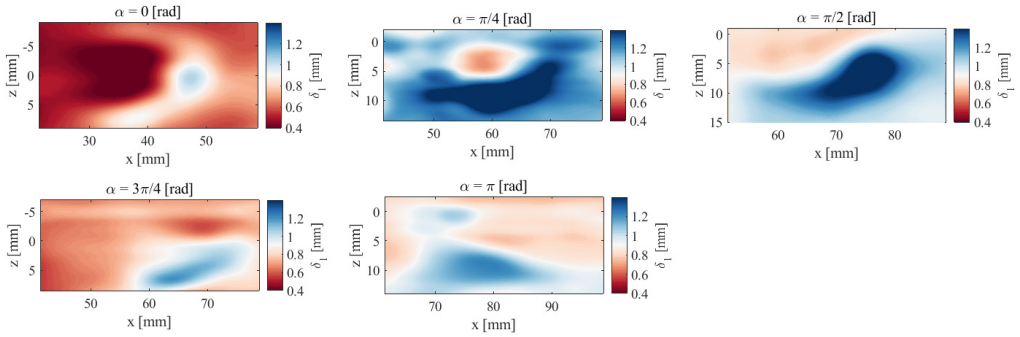

Figure 9. Boundary layer displacement thickness at t = 1 ms for various electrode sweep angles.

Figure 7 shows the distribution of the local momentum thickness in the disturbed boundary layer. One can see that a reduction in δ_1 in the major part of the interaction region is obtained only for the co-flow propagation of the arc. In this case, both the kinematic transport of the stream-wise momentum in the vortex and the initial acceleration of the flow due to Ampere force inject momentum into the bottom part of the boundary layer, and thus, decrease the momentum thickness.

3.4. Boundary Layer Thickness and Free-Stream Velocity Effect

The efficiency of any vortex generator is determined by the strength and position of the induced vortex in the boundary layer. The initial size of the vortex induced by the MHD actuator is approximately equal to the diameter of the heated cavern left after the pulse. To analyze the boundary layer thickness effect on the interaction, we performed a study of vortex evolution in a thick artificial boundary layer for the case $\alpha = 0$. For the boundary layer with a thickness of δ_{99} = 15 mm (δ_1 = 2.6 mm), the center of the vortex was located at a position of 0.3 δ_{99} from the wall. Taking the vortex core diameter, D, to be

approximately equal to 9 mm, we obtain (D/δ_{99}~0.6, D/δ_1 = 3.46). This case is in contrast with the experiments performed in a natural thin boundary layer with D/δ_{99}~1.2.

In Figure 10, we compare the position of the hairpin vortex head center and its dissipation in the boundary layer for the cases of D/δ_{99}~1.2 and D/δ_{99}~0.6. One can see that the increase in the boundary layer thickness leads to a higher convection speed of the disturbance. For the thicker boundary layer, we obtain a convection velocity $u/U_0 \sim 0.65$ compared to 0.9 for the natural one. This difference should lead to weaker stretching of the vortex in the former case. Also, one can see in Figure 10b that, at a higher D/δ, vortex decay is more intense. This is caused by higher turbulent dissipation for the submerged vortex.

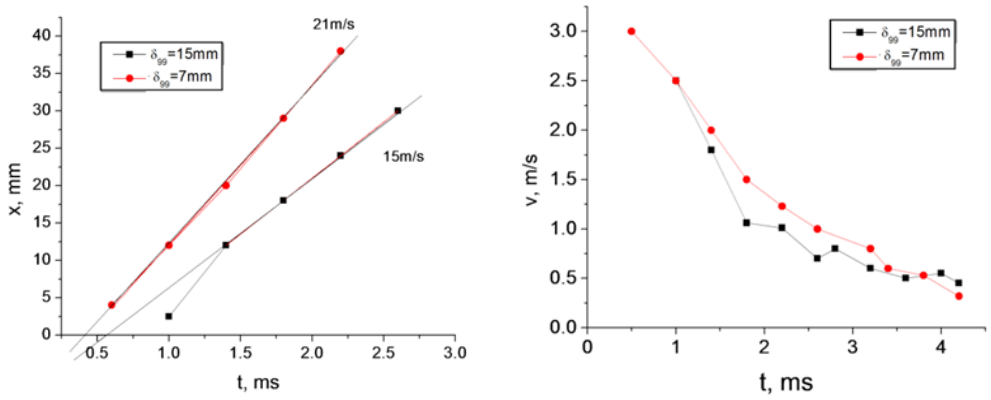

(**a**) (**b**)

Figure 10. Vortex head position (**a**) and its magnitude, defined as peak wall-normal velocity (**b**). t = 1 ms, $U_0 = 20$ m/s.

The modification of the boundary layer profile by the arc-induced hairpin vortex was studied up to a flow velocity of 80 m/s. The experiments were carried in the synthetic boundary layer formed by the obstacle array; thus, its thickness was held constant.

The flow structure in the symmetry plane is shown in Figure 11 for $U_0 = 35$ and 80 m/s. Disturbance is visualized via the stream-wise velocity component. One can see that both the disturbance structure and the boundary layer deformation do not principally depend on the flow velocity. A thinner boundary layer can be seen between the legs of the hairpin structure.

Stream-wise velocity excess is shown as a function of flow speed in Figure 11. One can see that, in the boundary layer with a constant thickness, the magnitude of the disturbance induced by the discharge increases with an increase in the flow velocity. This contradicts the intuitive assumption that a decrease in the momentum coefficient should reduce the disturbance magnitude.

The convective transport of stream-wise momentum, induced by a vortex in a boundary layer, can be estimated as

$$\frac{\Delta u}{\Delta t} \sim v\frac{\partial u}{\partial y} = v\frac{U_0}{\delta}k, \tag{2}$$

where $k \sim 0.6$ is introduced to account for the real local velocity gradient in the boundary layer in the region of the wall-normal velocity maximum.

The time present in (2) can be set as vortex dissipation time (see Figure 7). Then, the relative disturbance magnitude is given as

$$\frac{\Delta u}{U_0} \sim k\tau v\frac{1}{\delta}, \tag{3}$$

and remains constant for a constant convective velocity in the vortex and boundary layer parameters. The vertical velocity in the vortex, required to create an observed disturbance, is in the order of 10–20 m/s. It qualitatively corresponds to the typical velocity obtained

during the collapse of the hot cavern in the late stages of the current pulse [27]. The vortex intensity does not depend on the local flow velocity, since the momentum coefficient is rather high, $C_\mu > 1$, and the pulse duration is in the order of the convection time, $\tau = D/U_0 \sim 90$ µs, at $U_0 = 80$ m/s.

Variation in the flow velocity allows us to separate the role of the two mechanisms: acceleration of the flow by the Ampere force and vortex momentum transport. At low flow velocity, the amplitude of boundary layer perturbation at t = 1 ms tends to a constant value of 4 m/s. This corresponds to the local stream-wise velocity in the arc-induced vortex. This value corresponds to a direct addition of momentum by the Ampere force to the boundary layer. At higher flow velocities, boundary layer perturbation is caused by the "lift-up" of the boundary layer by the hairpin vortex, and thus, the velocity excess $\Delta u/U_0$ is held constant.

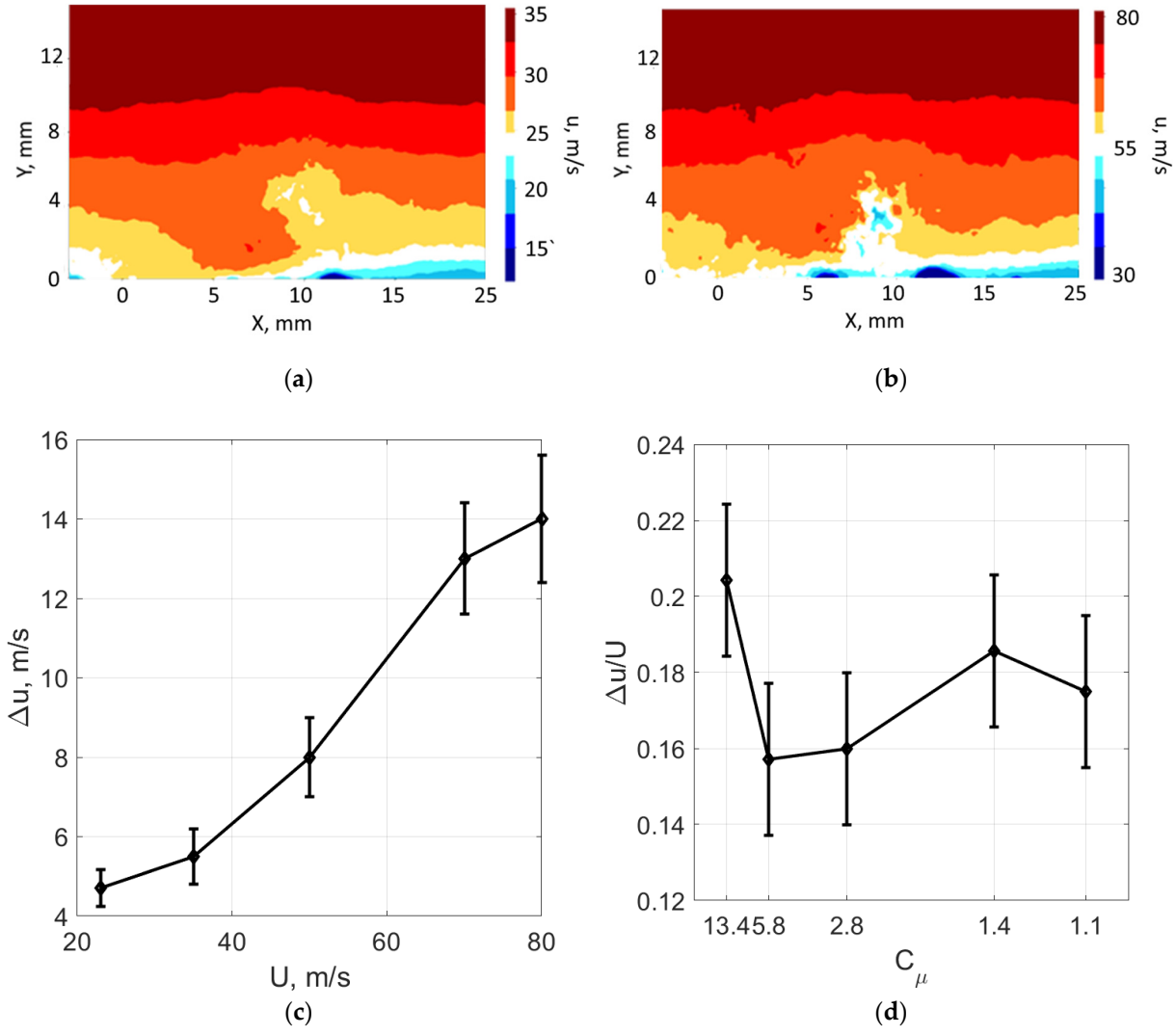

Figure 11. Stream-wise velocity field deformation at various free-stream flow velocities: (**a**) 35 m/s, (**b**) 70 m/s. (**c**) Magnitude of the boundary layer perturbation at increasing free-stream velocity. (**d**) Same as (**c**), in non-dimensional variables.

3.5. Boundary Layer Separation Control by MHD Actuator

Boundary layer separation was studied at flow velocities of 20 and 50 m/s. The boundary layer thickness in these cases was artificially increased up to δ_1 = 2.6 mm upstream of the trailing section of the bump.

The flow evolution for the two free-stream velocities is shown in Figures 12 and 13. The color palette was selected to visualize the separation line and has a maximal sensitivity at low velocities. After the breakdown, a vortex and an accelerated flow region are formed downstream of the actuator position. The dark region for time moments <0.5 ms corresponds to the hot unseeded cavern left after the breakdown.

For $U_0 = 20$ m/s (Figure 12), the separation point starts to move downstream immediately after the breakdown and stops 25 mm (1/2 H) downstream of the initial position at t = 1.5 ms. After that, the separation bubble propagates upstream, and the flow structure is restored approximately 6 ms after the pulse initiation.

For higher velocity, $U_0 = 50$ m/s, the flow evolution is similar, although the maximal shift of the separation point in this case is just 7 mm. The initial position of the separation point is restored in approximately 1 ms, and at t = 2 ms, it is followed by relaxation of the shear layer position.

The typical time of the flow relaxation can be recalculated to the Strouhal number using the free-stream velocity and bump height. This estimation gives Sh = 0.4 for 20 m/s and Sh = 0.5 for 50 m/s. These Sh values are consistent with the typical relaxation time of the separated flows.

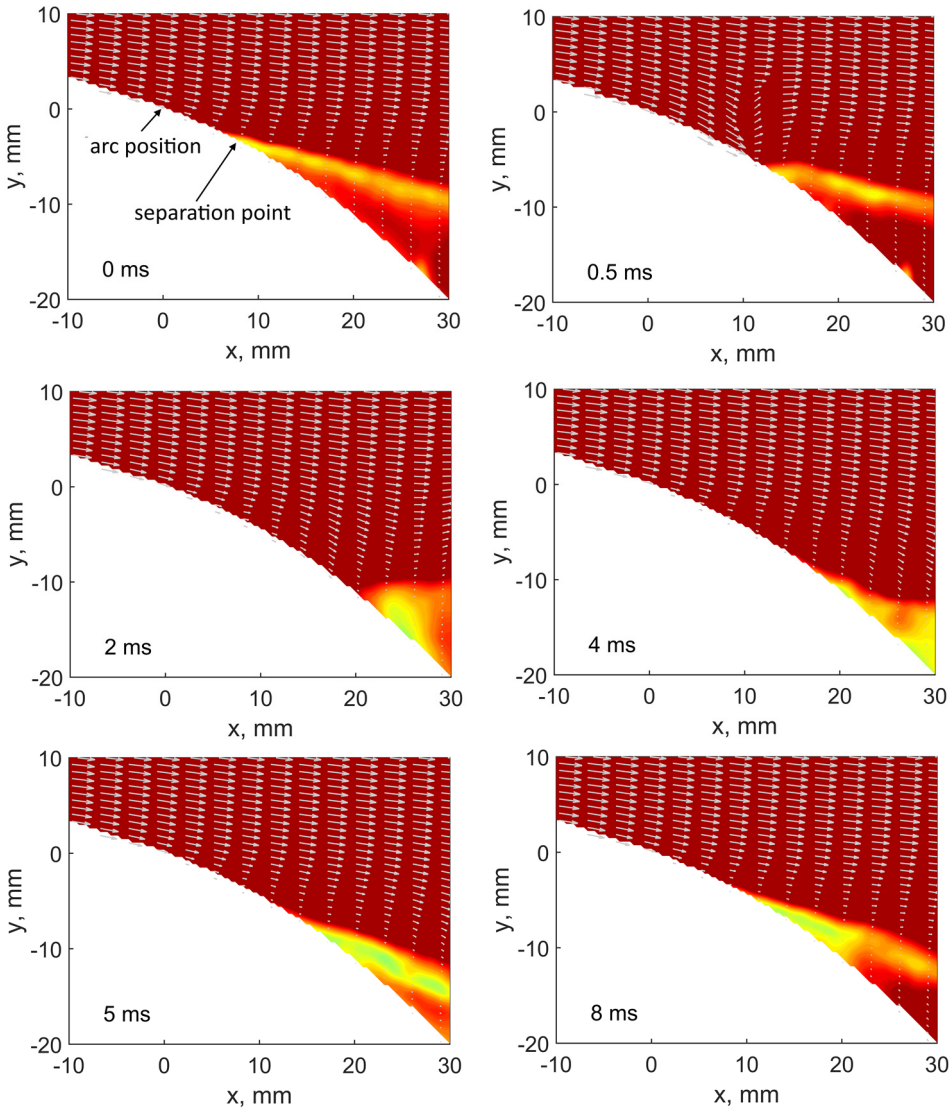

Figure 12. Separation line evolution after the MHD actuator pulse. $U_0 = 20$ m/s.

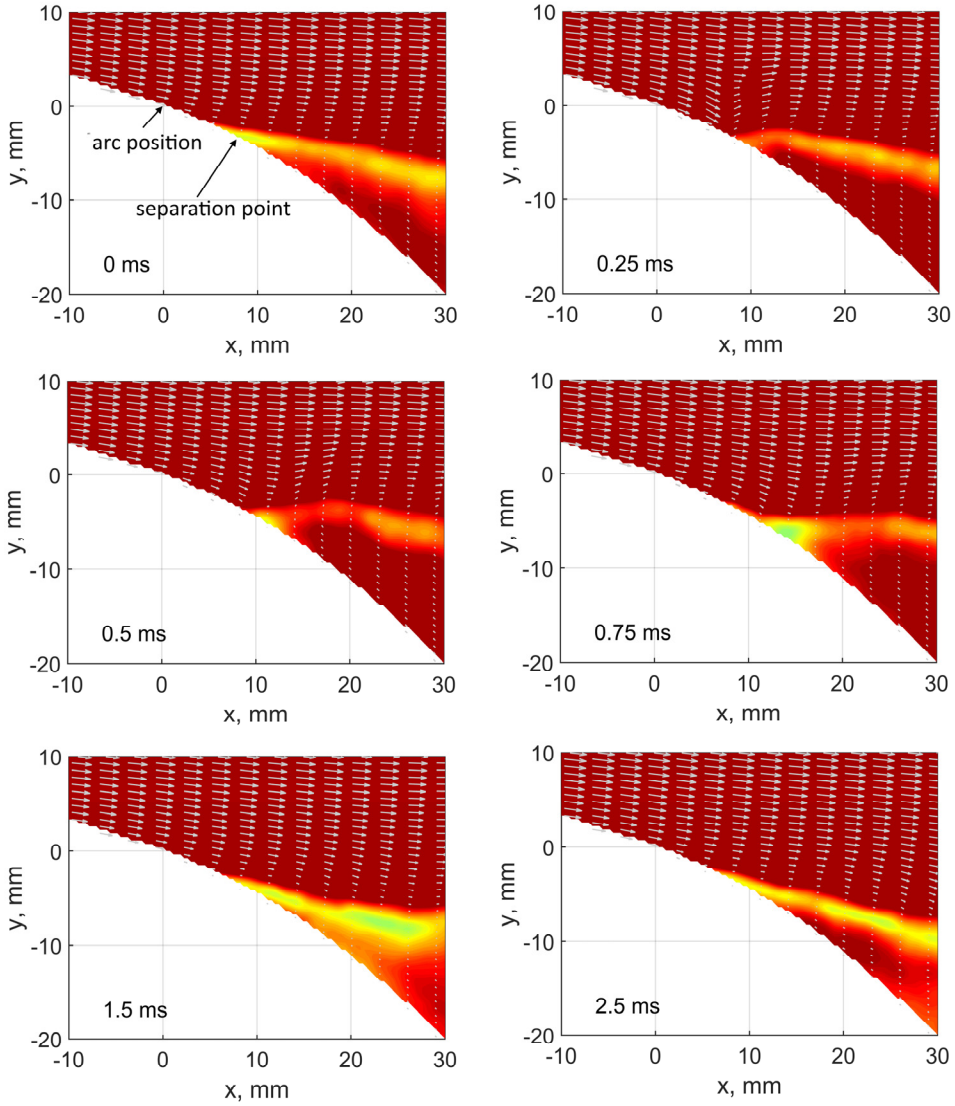

Figure 13. Separation line evolution after the MHD actuator pulse. $U_0 = 50$ m/s.

Finally, we examined the separation line shift when the actuator was operating in a pulse-repetitive mode. Again, the experiments were carried out at a flow velocity of 50 m/s and in a thick artificial boundary layer. The pulse repetition rates were 280 and 700 Hz, with individual pulse characteristics held roughly constant. The actuator operation parameters are summarized in Table 2. To exclude aliasing, laser frequency was chosen to obtain 20 images per actuator period, and up to 500 frames were averaged to obtain the average flow field.

Table 2. Actuator peak momentum coefficient in various flow conditions.

F, Hz	Sh	$<C_\mu>$	$<C_{\mu H}>$
280	0.3	0.044	2.4×10^{-3}
700	0.7	0.11	6×10^{-3}

Figure 14 shows the location of the separation line for the actuated and reference cases. One can see that for the high PRF and average momentum coefficient $<C_{\mu H}> = 0.6\%$, the average position of the separation line is shifted by approximately 7 mm. For the frequency of 280 Hz, oscillations of the separation region seem to smear the separation line position.

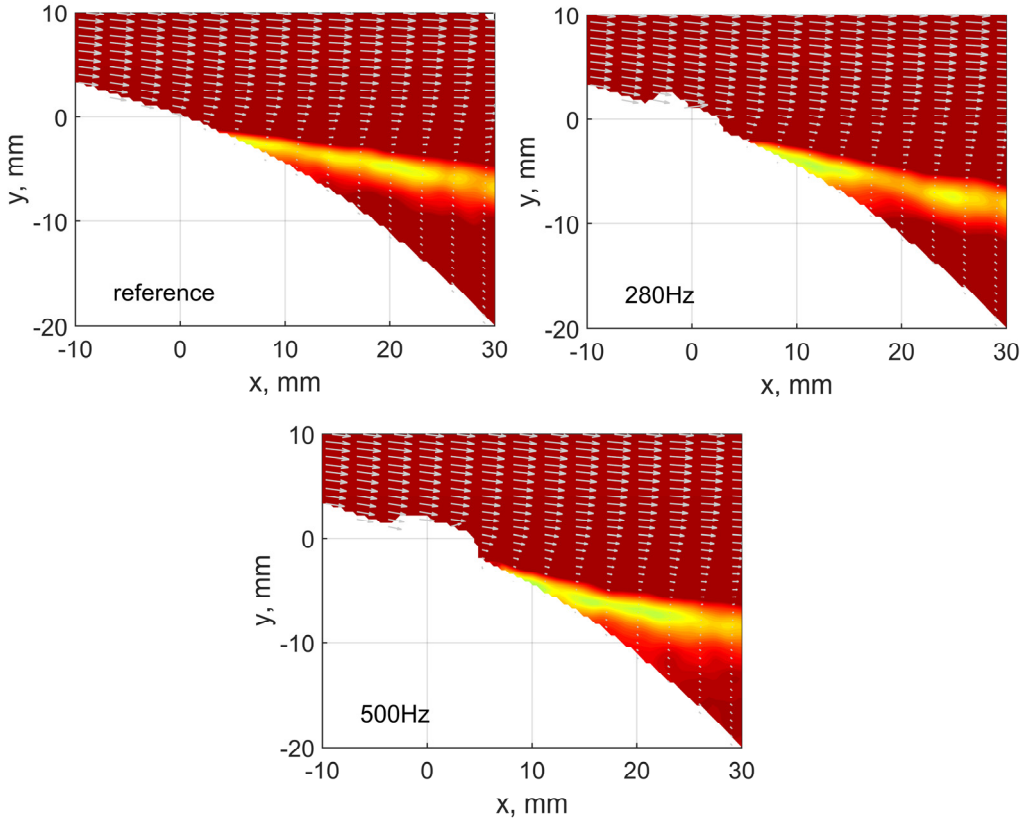

Figure 14. Position of the separation line for various pulse repetition rates. $U_0 = 50$ m/s.

The momentum coefficient, required to obtain measurable flow control, is comparable to the fluidic vortex generators, like zero-mass-flux jets or fluidic oscillators. Studies [30,31] report for these devices that a value in the order of 2% is required to control the separation line position. Also, one should note that the operation of the actuator array should have a greater average effect on the flow than the single-electrode section.

4. Conclusions

The electric arc in an eternal magnetic field was studied as an actuator for boundary layer separation control. Measurements were taken at subsonic flow velocities up to 80 m/s in a natural and an artificially created turbulent boundary layer. It is shown that the action of the pulsed Ampere force in the arc leads to the formation of a hairpin vortex near the wall. The evolution of this vortex is strongly affected by local shear and turbulent viscosity present in the boundary layer, and by the interaction of the vortex filaments in the hairpin legs.

The deformation of the boundary layer profile occurs due to both momentum transport in the hairpin vortex and MHD flow acceleration. The best effect is achieved when the arc propagates in the co-flow direction. The normalized magnitude of stream-wise velocity disturbances does not depend on the external flow velocity due to the high actuator momentum coefficient and short pulse duration. For the conditions studied in this work, the peak velocity excess observed in the boundary layer is in the order of 0.17 U_0 at 80 m/s and $C_\mu = 1.1$. For a velocity above 30 m/s, the kinematic momentum transport in the vortex dominates over the direct stream-wise momentum injection due to Ampere force.

Control of the flow separation on the smooth wall was attempted at flow velocities of 20 and 50 m/s. The reaction of the separation region on the actuator pulse involves a downstream shift of the separation point, followed by flow relaxation. The maximal shift of the separation point obtained is as high as 25 mm (half the height of the bump) for 20 m/s and 6 mm for 50 m/s. In the pulse-repetitive case, a measurable local reduction in the

separation region size is obtained at average momentum coefficients of $C_{\mu H} = 0.6\%$ and Sh = 0.7.

In general, MHD plasma actuators can be used for the manipulation of relatively thick boundary layers, with thicknesses comparable to the arc diameter (~2 mm). For these cases, they demonstrate separation control authority at a momentum coefficient of $C_{\mu H} = 0.6\%$, comparable to fluidic actuators. Further research, however, should include energetic efficiency estimation and feasibility studies for cases when these devices are used for separation control in turbulent flows.

Author Contributions: A.K.—investigation, data curation, writing; P.K.—investigation, methodology, writing; I.M.—methodology, writing, supervision. All authors have read and agreed to the published version of the manuscript.

Funding: This work was supported by the Ministry of Science and Higher Education of the Russian Federation (State Assignment No. 075-01129-23-00).

Data Availability Statement: The data presented in this manuscript are available from the authors upon reasonable request.

Conflicts of Interest: The authors declare no conflict of interest. The funders had no role in the design of the study; in the collection, analyses, or interpretation of the data; in the writing of the manuscript; or in the decision to publish the results.

Abbreviations

TBL	turbulent boundary layer
MHD	magnetohydrodynamics
PIV	particle image velocimetry
A	electrode sweep angle
Ω	vorticity
δ_1	displacement thickness
δ_{99}	total boundary layer thickness (at u = 99%U_0)
H	bump height
U_0	oncoming flow velocity
x, y, z X, Y, Z	co-ordinate system with a center in the center of the electrode gap
I	discharge current
B	magnetic field strength
F	pulse repetition rate
$C_\mu = IB/(\rho {U_0}^2 \delta_1)$	'local' momentum coefficient, based on boundary layer displacement thickness
$C_{\mu H} = IB/(\rho {U_0}^2 H)$	'global' momentum coefficient, based on bump height
$Sh = FH/U_0$	Strouhal number

References

1. Kriegseis, J.; Simon, B.; Grundmann, S. Towards In-Flight Applications? A Review on Dielectric Barrier Discharge-Based Boundary-Layer Control. *Appl. Mech. Rev.* **2016**, *68*, 020802. [CrossRef]
2. Wang, J.-J.; Choi, K.-S.; Feng, L.-H.; Jukes, T.N.; Whalley, R.D. Recent Developments in DBD Plasma Flow Control. *Prog. Aerosp. Sci.* **2013**, *62*, 52–78. [CrossRef]
3. Starikovskiy, A.Y.; Aleksandrov, N.L. Plasma Aerodynamics and Flow Control by Superfast Local Heating. In *Pulsed Discharge Plasmas: Characteristics and Applications*; Shao, T., Zhang, C., Eds.; Springer Nature: Singapore, 2023; pp. 939–1034, ISBN 978-981-99-1141-7.
4. Roth, J.R.; Sherman, D.M.; Wilkinson, S.P. Electrohydrodynamic Flow Control with a Glow-Discharge Surface Plasma. *AIAA J.* **2000**, *38*, 1166–1172. [CrossRef]
5. Roupassov, D.V.; Nikipelov, A.A.; Nudnova, M.M.; Starikovskii, A.Y. Flow Separation Control by Plasma Actuator with Nanosecond Pulsed-Periodic Discharge. *AIAA J.* **2009**, *47*, 168–185. [CrossRef]
6. Starikovskiy, A.; Meehan, K.; Miles, R.B. Dynamic Stall Control by NS SDBD Actuator. In Proceedings of the AIAA SciTech Forum, Kissimmee, FL, USA, 8–12 January 2018.
7. Post, M.L.; Corke, T.C. Separation Control Using Plasma Actuators: Dynamic Stall Vortex Control on Oscillating Airfoil. *AIAA J.* **2006**, *44*, 3125–3135. [CrossRef]

8. Sekimoto, S.; Kato, H.; Fujii, K.; Yoneda, H. In-Flight Demonstration of Stall Improvement Using a Plasma Actuator for a Small Unmanned Aerial Vehicle. *Aerospace* **2022**, *9*, 144. [CrossRef]
9. Sidorenko, A.; Budovsky, A.; Pushkarev, A.; Maslov, A. Flight Testing of DBD Plasma Separation Control System. In Proceedings of the 46th AIAA Aerospace Sciences Meeting and Exhibit, Reno, NV, USA, 7–10 January 2008; p. 373.
10. Correale, G.; Popov, I.B.; Rakitin, A.E.; Starikovskii, A.Y.; Hulshoff, S.J.; Veldhuis, L.L.M.; Starikovskiy, A.Y. Flow Separation Control on Airfoil With Pulsed Nanosecond Discharge Actuator. In Proceedings of the 49th AIAA Aerospace Sciences Meeting including the New Horizons Forum and Aerospace Exposition, Orlando, FL, USA, 4–7 January 2011; AIAA: Orlando, FL, USA, 2011; pp. 2011–1079.
11. Lin, J.C. Review of Research on Low-Profile Vortex Generators to Control Boundary-Layer Separation. *Prog. Aerosp. Sci.* **2002**, *38*, 389–420. [CrossRef]
12. Jukes, T.N.; Choi, K.-S. On the Formation of Streamwise Vortices by Plasma Vortex Generators. *J. Fluid Mech.* **2013**, *733*, 370–393. [CrossRef]
13. Wicks, M.; Thomas, F.O.; Corke, T.C.; Patel, M.; Cain, A.B. Mechanism of Vorticity Generation in Plasma Streamwise Vortex Generators. *AIAA J.* **2015**, *53*, 3404–3413. [CrossRef]
14. Schatzman, D.M.; Thomas, F.O. Turbulent Boundary-Layer Separation Control with Single Dielectric Barrier Discharge Plasma Actuators. *AIAA J.* **2010**, *48*, 1620–1634. [CrossRef]
15. Little, J.; Samimy, M. High-Lift Airfoil Separation with Dielectric Barrier Discharge Plasma Actuation. *AIAA J.* **2010**, *48*, 2884–2898. [CrossRef]
16. Popkin, S.H.; Cybyk, B.Z.; Foster, C.H.; Alvi, F.S. Experimental Estimation of SparkJet Efficiency. *AIAA J.* **2016**, *54*, 1831–1845. [CrossRef]
17. Enloe, C.; Corke, T.; Jumper, E.; Kachner, K.; McLaughlin, T.; Van Dyken, R. Mechanisms and Responses of a Single Dielectric Barrier Plasma Actuator: Plasma Morphology. *AIAA J.* **2004**, *42*, 589–594. [CrossRef]
18. Kriegseis, J.; Grundmann, S.; Tropea, C. Power Consumption, Discharge Capacitance and Light Emission as Measures for Thrust Production of Dielectric Barrier Discharge Plasma Actuators. *J. Phys. D Appl. Phys.* **2011**, *110*, 013305. [CrossRef]
19. Emerick, T.; Ali, M.Y.; Foster, C.; Alvi, F.S.; Popkin, S. SparkJet Characterizations in Quiescent and Supersonic Flowfields. *Exp. Fluids* **2014**, *55*, 1858. [CrossRef]
20. Belinger, A.; Hardy, P.; Gherardi, N.; Naude, N.; Cambronne, J.P.; Caruana, D. Influence of the Spark Discharge Size on a Plasma Synthetic Jet Actuator. *IEEE Trans. Plasma Sci.* **2011**, *39*, 2334–2335. [CrossRef]
21. Zong, H.; Kotsonis, M. Effect of Velocity Ratio on the Interaction between Plasma Synthetic Jets and Turbulent Cross-Flow. *J. Fluid Mech.* **2019**, *865*, 928–962. [CrossRef]
22. Polivanov, P.; Vishnyakov, O.; Sidorenko, A. Study of Plasma-Based Vortex Generator in Supersonic Turbulent Boundary Layer. *Aerospace* **2023**, *10*, 363. [CrossRef]
23. Kazanskii, P.N.; Moralev, I.A.; Kotvitskii, A.Y. Flow Separation Control on a Smooth Ledge Using an Arc Discharge in a Magnetic Field. *J. Phys. Conf. Ser.* **2021**, *2100*, 012012. [CrossRef]
24. Cowley, M.D. *A Boundary-Layer Model for Balanced Arcs*; NASA: Greenbelt, MD, USA, 1967.
25. Ahrens, F.W.; Powell, H.N. Effects of a Transverse Magnetic Field on a Constricted Electric Arc. *J. Heat Transfer* **1975**, *97*, 267–273. [CrossRef]
26. Moralev, I.; Kazanskii, P.; Bityurin, V.; Bocharov, A.; Firsov, A.; Dolgov, E.; Leonov, S. Gas Dynamics of the Pulsed Electric Arc in the Transversal Magnetic Field. *J. Phys. D Appl. Phys.* **2020**, *53*, 425203. [CrossRef]
27. Kazanskii, P.N.; Kotvitskii, A.Y.; Moralev, I.A. Three-Dimensional Flow Structure in the Vicinity of the Pulsed Surface Arc Discharge in a Magnetic Field. *Tech. Phys. Lett.* **2021**, *47*, 6–9. [CrossRef]
28. Zaidi, S.H.; Smith, T.; Macheret, S.; Miles, R.B. Snowplow Surface Discharge in Magnetic Field for High Speed Boundary Layer Control. In Proceedings of the 44th AIAA Aerospace Sciences Meeting and Exhibit, Reno, NV, USA, 9–12 January 2006.
29. Repik, E.; Sosedko, Y. *Management of Free-Stream Turbulence*; Fizmathlit: Moscow, Russia, 2002; ISBN 5-94052-055-3. (In Russian)
30. Schmidt, H.J.; Woszidlo, R.; Nayeri, C.N.; Paschereit, C.O. Separation Control with Fluidic Oscillators in Water. *Exp. Fluids* **2017**, *58*, 106. [CrossRef]
31. Cerretelli, C.; Kirtley, K. Boundary Layer Separation Control with Fluidic Oscillators. *J. Turbomach.* **2009**, *131*, 041001. [CrossRef]